Effects of energy correlations and superexchange on charge transport and exciton formation in amorphous molecular semiconductors: An *ab initio* study

Andrea Massé,[1] Pascal Friederich,[2] Franz Symalla,[2] Feilong Liu,[1] Velimir Meded,[2] Reinder Coehoorn,[1,3] Wolfgang Wenzel,[2] and Peter A. Bobbert[1,*]

[1]*Department of Applied Physics, Technische Universiteit Eindhoven, P.O. Box 513, NL-5600 MB Eindhoven, The Netherlands*

[2]*Institute of Nanotechnology, Karlsruhe Institute of Technology (KIT), D-76344 Eggenstein-Leopoldshafen, Germany*

[3]*Institute for Complex Molecular Systems, Technische Universiteit Eindhoven, P.O. Box 513, NL-5600 MB Eindhoven, The Netherlands*

(Received 9 January 2017; published 31 March 2017)

In this study, we investigate on the basis of *ab initio* calculations how the morphology, molecular on-site energies, reorganization energies, and charge transfer integral distribution affect the hopping charge transport and the exciton formation process in disordered organic semiconductors. We focus on three materials applied frequently in organic light-emitting diodes: α-NPD, TCTA, and Spiro-DPVBi. Spatially correlated disorder and, more importantly, superexchange contributions to the transfer integrals, are found to give rise to a significant increase of the electric field dependence of the electron and hole mobility. Furthermore, a material-specific correlation is found between the HOMO and LUMO energy on each specific molecular site. For α-NPD and TCTA, we find a positive correlation between the HOMO and LUMO energies, dominated by a Coulombic contribution to the energies. In contrast, Spiro-DPVBi shows a negative correlation, dominated by a conformational contribution. The size and sign of this correlation have a strong influence on the exciton formation rate.

DOI: 10.1103/PhysRevB.95.115204

I. INTRODUCTION

A thorough understanding of the electronic properties of amorphous molecular semiconductors is crucial for the further development of organic devices based on these semiconductors, such as organic light-emitting diodes (OLEDs), organic photovoltaic devices, and (light-emitting) organic field-effect transistors. An acceleration in this understanding has occurred by the employment of *ab initio* calculations of the morphology and the intermolecular charge hopping rates of these semiconductors [1–6]. Recently, we developed an *ab initio* model for hole transport in two amorphous molecular semiconductors often used as hole transporters in OLEDs: α-NPD [N,N'-Di(1-naphthyl)-N,N'-diphenyl-(1, 1'-biphenyl)-4,4'-diamine] and TCTA [tris(4-carbazoyl-9-ylphenyl)amine] [7]. In the model, we treated the Gaussian disorder in the molecular on-site hole energies as spatially uncorrelated. We justified this by the rather low degree of spatial energy correlations found in the *ab initio* calculations. The low degree of correlation was attributed to the vanishing molecular dipole moment of the α-NPD and TCTA molecules. The conclusion was that in both materials the calculated hole mobility $\mu(T,c,F)$ as a function of temperature T, hole concentration c, and electric field F could be quite accurately described by the parametrization scheme of the extended Gaussian disorder model (EGDM) [8], with slightly different parameters for the T and F dependence. The EGDM accounts in addition to the dependence of μ on T and F as included in the Gaussian disorder model (GDM) [9] also for the dependence on carrier concentration c.

For the case of α-NPD, we used the parameterized hole mobility function in one-dimensional drift-diffusion modeling of the T-dependent current density-voltage (J-V) characteristics of two types of hole-only devices [7]. It was found that for both types of devices these characteristics could be quite well described by only adjusting the calculated value $\sigma = 0.13$ eV of the standard deviation of the Gaussian energy disorder to 0.10 eV. Following up on this work, we recalculated σ by using instead of the standardized force field in Ref. [7] a material-specific force field in the morphology calculation, resulting in $\sigma = 0.087$ eV [10]. We found that with this value it was possible to quite well model T-dependent J-V as well as impedance spectroscopy data of hole-only devices consisting of undoped α-NPD layers sandwiched in between highly p-doped α-NPD layers. Also, the discrepancy with the measured time-of-flight (TOF) mobility of holes in α-NPD reported in Ref. [7] was resolved in Ref. [10]. Agreement between the hole mobility in α-NPD extracted from device simulations and measured by TOF was reported previously by Schwartz *et al.* [11]. In another TOF study of hole transport in α-NPD, the value $\sigma = 0.090$ eV was found from a fit to the GDM of the T dependence of the mobility [12], in excellent agreement with the value of $\sigma = 0.087$ eV. In Ref. [10], a refined modeling as compared to Ref. [7] was employed, including a series resistance and an adjusted dielectric constant of α-NPD, both extracted from the impedance spectroscopy data, and a full three-dimensional treatment of the hole transport in the undoped α-NPD layers. Although the overall agreement between modeled and measured data was quite good, both in Refs. [7,10] the experimental J-V curves were consistently steeper than the modeled curves, pointing at an underestimation of the F dependence of μ.

It is well known that spatial correlation between the on-site energies can strongly increase the F dependence of μ, an effect that is accounted for in the correlated disorder model (CDM) [13,14]. For the case that the on-site energies are fully determined by the electrostatic interaction of a charge with randomly oriented dipoles located at the sites, the extended correlated disorder model (ECDM) was developed [15]. The ECDM accounts, similarly to the EGDM, in addition to the T and F dependence also for the c dependence of μ. Because of the vanishing molecular dipole moment of α-NPD

*p.a.bobbert@tue.nl

and TCTA, the ECDM is not applicable to these materials. Numerical studies of charge transport in the electron transporter Alq_3 [tris(8-hydroxyquinolinato)aluminium] [16] and the hole transporter DPBIC [tris[(3-phenyl-1H-benzimidazol-1-yl-2(3H)-ylidene)-1,2-phenylene]Ir] [6], which both have a large dipole moment, show that the energy autocorrelation function for large distance r deviates from the $1/r$ dependence of the dipole-induced correlation function of the ECDM. Hence, even in the case of molecular semiconductors with a large molecular dipole moment, the ECDM appears to be inapplicable.

In the present work, we will employ a simplified version of the model proposed in Ref. [16] to describe the spatial energy correlation. We will then quantify, based on similar *ab initio* calculations as in Refs. [7,10], the effect of the weak spatial energy correlations on both the electron and hole mobility functions of α-NPD, TCTA, and Spiro-DPVBi [2,2',7,7'-tetrakis(2,2-diphenylvinyl)Spiro-9,9'-bifluorene]. In the latter material, which is used as a blue fluorescent emitter in OLEDs [17], both electron and hole transport are important [18].

Another effect that can lead to an enhancement of the F dependence of μ is superexchange, which is the indirect electronic coupling between orbitals localized on two sites via virtual orbitals on intermediate sites [19–21]. We recently established from *ab initio* calculations that including superexchange coupling of guest orbitals via virtual host orbitals leads to a strong enhancement and change in the guest concentration dependence of the hole mobility in two prototypical host-guest systems often used as emitting layers in OLEDs [18]: α-NPD:Ir(MDQ)2(acac) (α-NPD doped with the red-emitting dye (acelylacetonate)bis(2-methyldibenzo[f,h]quinoxinalate)iridium) and TCTA:$Ir(ppy)_3$ (TCTA doped with the green-emitting dye fac-tris(2-phenylpyridyl)iridium) [22]. Although in pure α-NPD and TCTA a similarly strong enhancement of the mobility is not expected, the longer hopping range associated with superexchange is expected to enhance its F dependence. We will include the effect of superexchange to lowest order in a similar way as in Ref. [22] and quantify its influence on the F dependence of the electron and hole mobilities for the three materials mentioned above.

The *ab initio* calculations of the energies of the highest occupied molecular orbital (HOMO) and lowest unoccupied molecular orbital (LUMO) required to address the effects of spatial energy correlations and superexchange also allow us to investigate the molecular on-site correlation between HOMO and LUMO energies. The existence of on-site HOMO-LUMO energy correlation and its sign are of importance for the rate of exciton formation [23]. In the case of positive HOMO-LUMO energy correlation (negative correlation between electron and hole energies in the terminology used in Ref. [23]), the probability that electrons and holes are trapped at different sites is larger than in the case of negative HOMO-LUMO energy correlation (positive correlation between electron and holes energies). This leads to a lower exciton formation rate for positive than for negative HOMO-LUMO energy correlation. We note that in Ref. [23] the exciton binding energy was assumed to be sufficiently large to prevent unbinding of the exciton, so that effects of a finite exciton binding energy and its possible correlation with the LUMO and HOMO energies were not included.

This paper is organized as follows. In Sec. II, we briefly recapitulate our *ab initio* microscopic calculations of the morphology, site energies, reorganization energies, and charge transfer integrals, as well as the stochastic expansion method used to expand the obtained microscopic information to large simulations boxes for master-equation mobility calculations equivalently to those in Ref. [7]. In Secs. III and IV, we discuss the way in which we include spatial energy correlations and superexchange, respectively. In Sec. V, we discuss the results for the electron and hole mobility functions of α-NPD, TCTA, and Spiro-DPVBi obtained from the master-equation calculations. The mobility functions can be quite well described by the parametrization scheme given in Refs. [7,8], with adapted parameters for the T and c dependence. We find that the most important effect of including weak spatial energy correlations and superexchange is an increase of the F dependence of μ, with the effect of including superexchange being the most significant. In Sec. VI, we present the results for the on-site HOMO-LUMO energy correlation in the three considered materials and provide an analysis of these results. For α-NPD and TCTA, we find a positive correlation dominated by a Coulombic contribution, while for Spiro-DPVBi we find a negative correlation dominated by a conformational contribution. Section VII contains a summary, the main conclusions, and a discussion.

II. *AB INITIO* CALCULATIONS AND STOCHASTIC EXPANSION METHOD

The *ab initio* calculations of the morphologies, site energies, reorganization energies, and charge transfer integrals for the three materials were performed in a similar way as in Refs. [7,10]. Morphologies at 300 K were obtained using the METROPOLIS Monte Carlo based simulated annealing protocol DEPOSIT [4], which was applied to simulate the deposition of about 1000 molecules in the vertical direction in simulation boxes of a lateral size of 7×7 nm^2 with periodic boundary conditions in the lateral directions. Site positions, defined as the molecular centers of mass, were obtained from a slab of this box with a height of 20 nm, avoiding surface effects. The resulting site densities are $N_t = 0.96$, 0.87, and 0.60 nm^{-3} for α-NPD, TCTA, and Spiro-DPVBi, respectively.

In the calculations of the electron and hole site energies, transfer integrals, and reorganization energies, the morphology simulation boxes were periodically repeated in the lateral directions. A spherical subsystem of about 3500 molecules was then considered. In the center of this subsystem, 1000 molecules were selected, for which the electron and hole site energies were obtained using the quantum patch embedding method described in Ref. [5]. The remaining 2500 molecules in the spherical subsystem were used as an electrostatic background. Within the group of 1000 molecules, an inner region with 200 molecules was considered for the calculation of the transfer integrals. These transfer integrals were calculated based on self-consistently evaluated molecular frontier orbitals using the Löwdin orthogonalization [24,25]. The Fock and overlap matrices were extracted from dimer calculations including environment embedding. Both site energies and transfer integrals were calculated with the Turbomole package [26] using a B3LYP functional

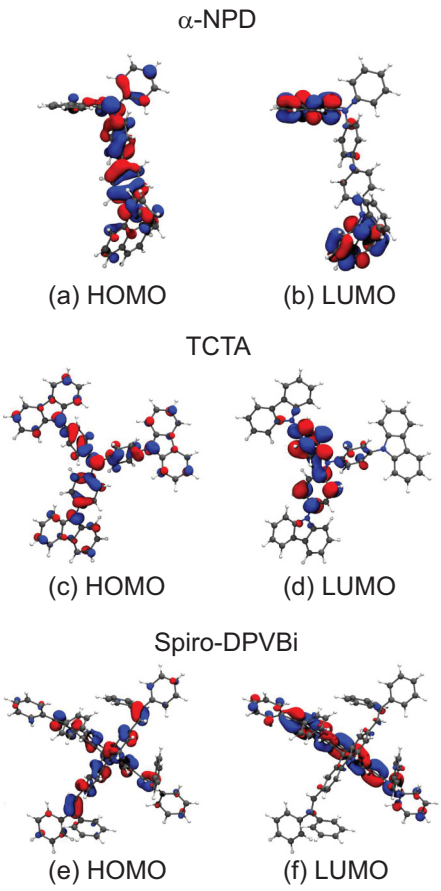

FIG. 1. Isosurfaces (blue: $+0.03a_0^{-3/2}$, red: $-0.03a_0^{-3/2}$, with a_0 the Bohr radius) of the HOMO and LUMO of α-NPD, TCTA, and Spiro-DPVBi in vacuum.

[27] and a def2-SV(P) basis set [28]. The electron and hole reorganization energies of molecules in this box were calculated using Nelsen's four-point-procedure [29] with a B3LYP functional and a def2-TZVP basis set in TURBOMOLE [30].

The site energies for both electrons and holes, i.e., the LUMO and HOMO energies, are in very good approximation distributed according to a Gaussian density of states (DOS). In the case of electrons, the standard deviations of the Gaussian DOS are $\sigma = 0.087$, 0.100, and 0.156 eV for α-NPD, TCTA, and Spiro-DPVBi, respectively. For holes, the values are $\sigma = 0.087$, 0.136, and 0.122 eV. The statistical uncertainty in these numbers is a few thousandths of an eV. The reorganization energies for electrons and holes vary in the amorphous system from molecule to molecule by a few hundredths of an eV. We do not take into account these small variations and instead fix the reorganization energies of all molecules at their average value, which is $E_r = 0.142$, 0.139, and 0.303 eV for electrons, and $E_r = 0.203$, 0.257, and 0.224 eV for holes. We neglect the relaxation energy of the environment around a charged molecule. Because of the fixed orientation of molecules in the condensed state, this relaxation energy is expected to be very small. Figure 1 shows the spatial structure of the HOMO and LUMO of the three considered molecules as obtained in vacuum.

We employ exactly the same stochastic methods as explained in Ref. [7] for the expansion of the morphologies and the generation of transfer integrals for the expanded morphologies, using the microscopic information from the above *ab initio* calculations as input. This stochastic expansion method allows us to generate site distributions (representing molecular centers of mass) according to the microscopically calculated morphologies and charge transfer integrals in between these sites for arbitrarily large simulation boxes. Electron and hole mobilities are then extracted from master-equation calculations of charge transport in simulation boxes much larger than those used in the *ab initio* calculations, in exactly the same way as in Ref. [7].

III. SPATIAL ENERGY CORRELATIONS

In Fig. 2, we plot the average $\langle \Delta E^2 \rangle^{1/2} \equiv \langle (E_i - E_j)^2 \rangle^{1/2}$ of the difference of LUMO [electron, Fig. 2(a)] and HOMO [hole, Fig. 2(b)] energies for all sites i and j with a mutual distance smaller than R in the microscopic samples for which

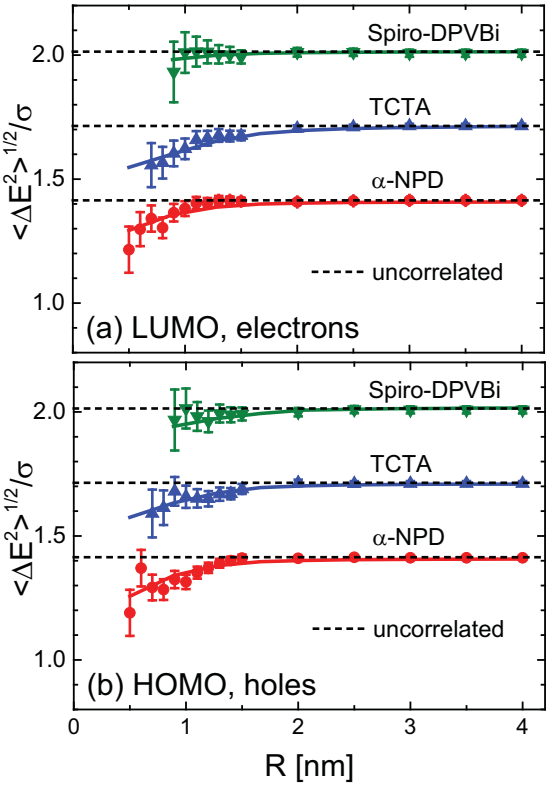

FIG. 2. Degree of spatial correlation between (a) LUMO (electron) and (b) HOMO (hole) energies at sites representing molecular centers of mass with a distance smaller than R, for α-NPD, TCTA, and Spiro-DPVBi. Symbols: results of microscopic *ab initio* calculations, averaged over 7 (α-NPD) and 3 (TCTA and Spiro-DPVBi) samples of 1000 molecules. Full curves: results for the correlated energy disorder model Eq. (1) in expanded $40 \times 40 \times 40$ nm^3 boxes, with the parameters listed in Table I. Dashed lines: no correlations. Offsets of 0.3 and 0.6 have been applied to the results for TCTA and Spiro-DPVBi, respectively. Because of improvements in the calculations, the results for the cases of holes in α-NPD and TCTA slightly differ from those shown in Fig. 1 of Ref. [7].

the *ab initio* calculations were performed. The deviation from the value $\sqrt{2}\sigma$, indicated by the dashed lines, is a measure for the degree of spatial energy correlation. For the cases of holes in α-NPD and TCTA considered by us in Ref. [7], it was concluded that the correlation is much weaker than for dipole-correlated disorder and the correlation was henceforth neglected. We conclude that for all considered cases in Fig. 2 the correlation is weak, both for electrons and holes. The correlation between energies at sites with the shortest mutual distance, which is a measure for the size of the molecule, appears to decay with increase of this distance in the order α-NPD–TCTA–Spiro-DPVBi.

We take into account the spatial energy correlations by a method similar to that of Baumeier *et al.*, applied by these authors to Alq_3 [16]. This organic semiconductor shows strong spatial energy correlations due to the large electric dipole moment of the Alq_3 molecule. The materials considered by us have a vanishing molecular dipole moment and the degree of correlation is therefore significantly lower than in Alq_3. Because of this, we use a simplified version of the method described in Ref. [16] based on a moving-average procedure developed by Thiedmann *et al.* [31], which is sufficient to reproduce the weak short-range correlations observed in Fig. 2. In this method, an energy E_i at site i is, apart from an offset average energy, calculated as

$$E_i = \sqrt{w} M_i^a + \sqrt{\frac{1-w}{n}} \sum_{j=1}^{n} M_j^b. \tag{1}$$

Here, M_i^a and M_i^b are two sets of independent random energies drawn from a Gaussian distribution with zero mean and standard deviation σ as obtained from the *ab initio* calculations, n is the number of nearest neighbors of site i taken into account, with site i itself added, and w and $1-w$ are weights for the two components of the right hand side of Eq. (1), where $0 < w < 1$.

The first component in Eq. (1) represents a spatially uncorrelated site energy distribution, whereas the second component introduces spatial correlation. The parameter w controls the strength of this correlation, while n controls its range. We determined the values of the parameters w and n such that the correlations in Fig. 2 as found in the *ab initio* calculations are well reproduced by site energies chosen according to Eq. (1) in a large box of $40 \times 40 \times 40$ nm^3 with stochastically generated site positions. The used parameters are listed in Table I and the corresponding energy correlations are given by the full curves in Fig. 2.

TABLE I. Parameters used in Eq. (1) to model the spatial energy correlations of the LUMO (electrons) and HOMO (holes) in α-NPD, TCTA, and Spiro-DPVBi, as shown in Fig. 2.

Material	Molecular orbital	w	n
α-NPD	LUMO	0.80	2
α-NPD	HOMO	0.75	2
TCTA	LUMO	0.75	4
TCTA	HOMO	0.80	3
Spiro-DPVBi	LUMO	0.90	2
Spiro-DPVBi	HOMO	0.85	2

IV. SUPEREXCHANGE

Superexchange is the indirect electronic coupling between orbitals localized on two sites via virtual orbitals on intermediate sites [19–21]. We include superexchange perturbatively to lowest order in the direct charge transfer integrals $J_{ik,0}$ between two molecular sites i and k in the same way as in Ref. [22]:

$$J_{ik} \cong J_{ik,0} + \sum_j \frac{J_{ij,0} J_{jk,0}}{\Delta E_{ijk}}, \tag{2}$$

with ΔE_{ijk} given by

$$\Delta E_{ijk} \equiv E_j - \frac{E_i + E_k}{2} + \frac{E_r}{2}. \tag{3}$$

Equation (3) has its particular form because the energies E_i, E_j, and E_k are those of the conformationally reorganized states with a charge on molecules i, j, and k, respectively. In the superexchange transfer from i to k, however, the charge is never actually located at the intermediate molecule j, so that the conformation of this molecule does not change [22]. To obtain the rate ω_{ik} for transfer of a charge from site i to k, the total charge transfer integral J_{ik} is inserted in the Marcus formula [32]:

$$\omega_{ik} = \frac{2\pi}{\hbar} \frac{J_{ik}^2}{\sqrt{4\pi E_r k_B T}} \exp\left[- \frac{(\Delta E_{ik} - E_r)^2}{4 E_r k_B T} \right], \tag{4}$$

where $\Delta E_{ik} \equiv E_k - E_i$.

In the calculation of the superexchange contribution to the total charge transfer integral in Eq. (2), we considered for each site only the largest 16 direct transfer integrals with other sites, which was checked to be more than sufficient in the subsequent charge-carrier mobility calculations. We note that in all calculations we disregarded occupation of other orbitals than the LUMO or HOMO, and also superexchange via other orbitals than those. Disregarding occupation of other orbitals than LUMO or HOMO may be justified by the fact that the percolative charge transport in amorphous molecular semiconductors involves only states in the low-energy tail of the DOS below a critical energy of the order of -0.5σ or lower [33]. With energies of the LUMO+1 (HOMO−1) that are typically 0.1 eV or more higher (lower) than that of the LUMO (HOMO) and values of σ of the order of 0.1 eV, the number of LUMO+1 (HOMO−1) states in this low-energy tail that is available in addition to the LUMO (HOMO) states is not expected to enhance the mobility significantly. The superexchange via energetically higher (lower) lying orbitals than the LUMO (HOMO) is suppressed by the factor ΔE_{ijk} in the denominator of the superexchange contribution in Eq. (2). Since this suppression is not very strong, significant corrections could be expected when including other orbitals than the LUMO (HOMO) as virtual orbitals in the superexchange.

Also, higher-order superexchange contributions involving more than one intermediate site could be included. Including such higher-order contributions would quickly lead to excessive computation times, because of the rapidly increasing number of combinations of intermediate sites. We therefore refrained from going beyond the lowest order in Eq. (2). In view of the neglect of higher-order contributions and of orbitals other than LUMO or HOMO in the superexchange

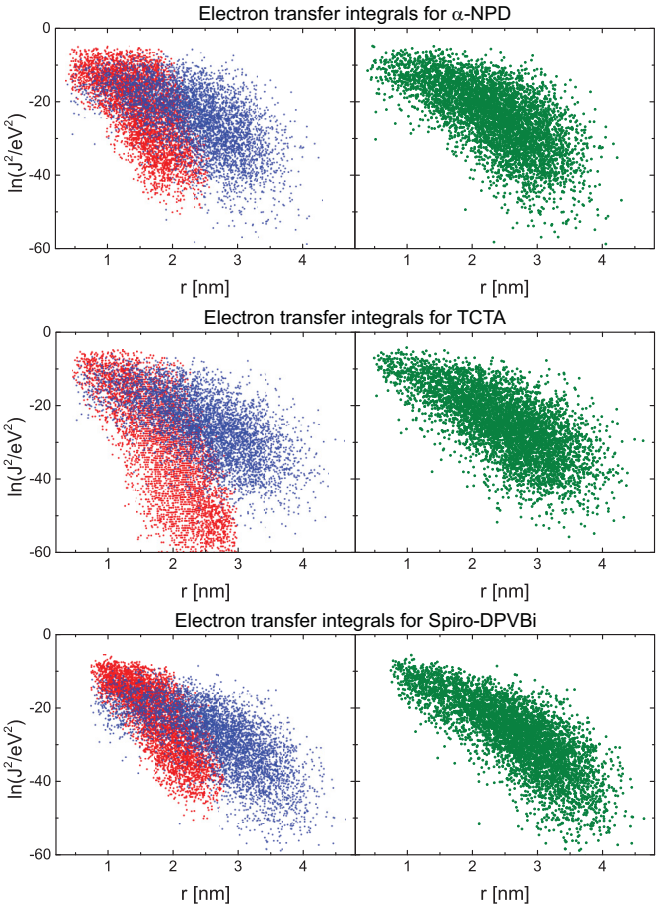

FIG. 3. Squared electron transfer integrals between molecular sites as a function of intersite distance r in $40 \times 40 \times 40$ nm^3 stochastically expanded simulation boxes representing the three considered materials. (Left) Separate squared direct (red points) and superexchange (blue points) contributions in Eq. (2). (Right) Squared total transfer integrals. For graphical reasons, each data set contains 5000 representative transfer integrals randomly chosen from the original data set.

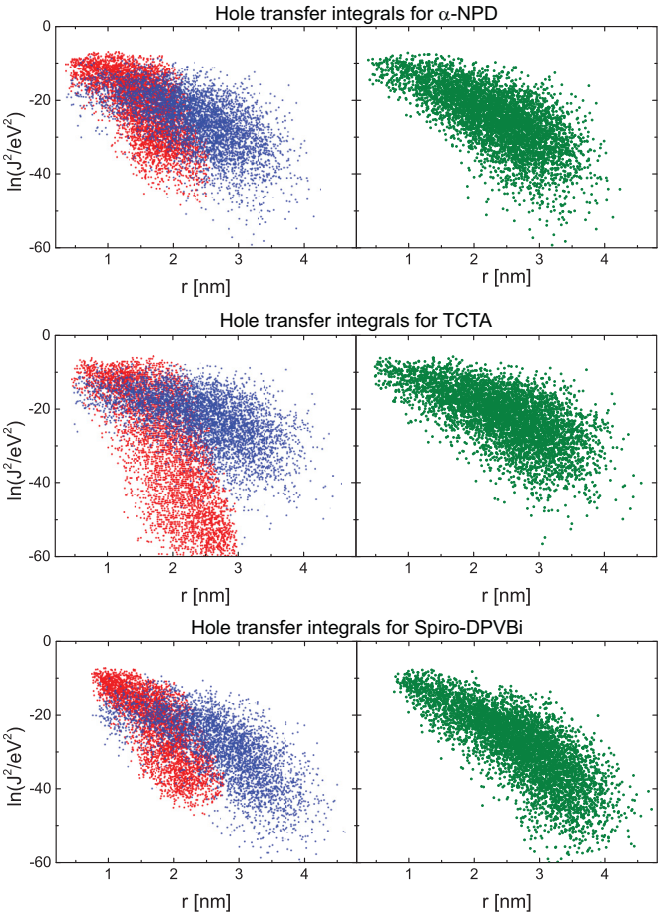

FIG. 4. Same as Fig. 3, but for holes.

our calculations are expected to provide a lower bound to the mobility increase by superexchange.

We remark that in Eq. (2) the relative signs of the transfer integrals start to matter with the inclusion of superexchange. In the *ab initio* calculations we find for all cases a division of close to 50%-50% between positive and negative transfer integrals. In the stochastic expansion method, we therefore attribute a random sign to the direct transfer integrals in Eq. (2). We also remark that the perturbation theory underlying Eq. (2) starts to fail when the denominator ΔE_{ijk} in the superexchange term is of the order of or smaller than either $J_{ij,0}$ or $J_{jk,0}$ (in terms of absolute values). For the rare combinations of sites for which this occurs, a regularization procedure is necessary. We replace in such case ΔE_{ijk} by either $J_{ij,0}$ or $J_{jk,0}$ (not changing its original sign). Other, more sophisticated, regularization procedures are possible, but this procedure is computationally convenient and was checked to be sufficient.

Figures 3 and 4 show for electrons and holes, respectively, the squares of the direct transfer integrals, the superexchange contribution in Eq. (2), and their sum as a function of distance. The importance of the superexchange coupling is clearly seen in all cases. It leads to significant couplings for rather large distances of 3–4 nm, where direct couplings have become negligible.

V. MOBILITY FUNCTIONS

The mobility functions $\mu(T,c,F)$ for electrons and holes in α-NPD, TCTA, and Spiro-DPVBi were obtained by solving a three-dimensional steady-state master equation for the charge-carrier occupational probabilities of the sites in large simulation boxes, in the same way as in Ref. [7]. The site positions and direct transfer integrals in the simulation boxes were stochastically generated using the methods as described in Ref. [7]. Spatial energy correlations were introduced according to the method described in Sec. III. The transfer integrals including superexchange coupling were obtained with the approach described in Sec. IV, using stochastically generated direct transfer integrals. We used simulation boxes with sizes up to $110 \times 110 \times 110$ nm^3 and performed averages over five disorder realizations, yielding results for the mobilities with sufficiently small error bars.

The resulting mobility functions $\mu(T,c,F)$ could all be fitted quite well with the parametrization scheme employed in Refs. [7,8], which involves a factorization of the c and F

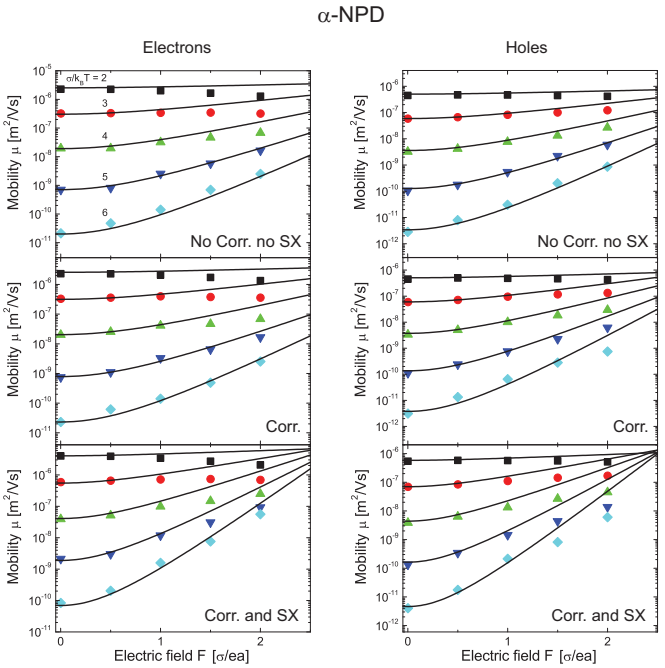

FIG. 5. Dependence of μ on electric field F for electrons (left) and holes (right) in α-NPD at a carrier concentration $c = 10^{-6}$ for different values of σ/k_BT. Symbols: master-equation results (error bars comparable to the symbol size or smaller). Curves: parametrization scheme Eqs. (5)–(9) with $A = 0.30$ and other parameters as given in Table II. Results are given for the cases with neither spatial energy correlations nor superexchange included (no Corr. no SX), only correlations included (Corr.), and both correlations and superexchange included (Corr. and SX).

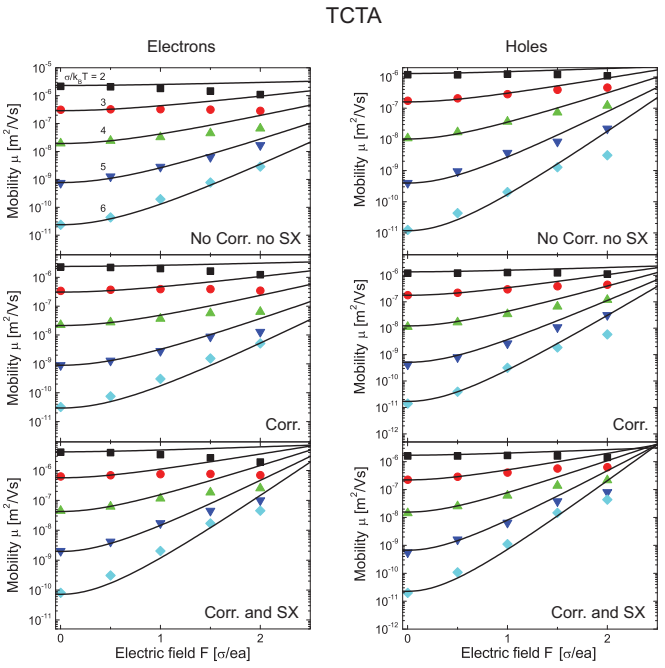

FIG. 6. Same as Fig. 5, but for TCTA.

dependence:

$$\mu(T,c,F) = \mu(T,c) f(T,F), \tag{5}$$

with

$$\mu(T,c) = \mu_0(T) \exp\left[\tfrac{1}{2}(\hat{\sigma}^2 - \hat{\sigma})(2c)^{\delta}\right], \tag{6}$$

$$\delta \equiv 2\frac{\ln(\hat{\sigma}^2 - \hat{\sigma}) - \ln(\ln 4)}{\hat{\sigma}^2}, \hat{\sigma} \equiv \frac{\sigma}{k_BT}, \tag{7}$$

$$\mu_0(T) = \mu_0^* \exp[-C\hat{\sigma}^2], \tag{8}$$

and

$$f(T,F) = \exp\left[A(\hat{\sigma}^{3/2} - 2.2)\left(\sqrt{1 + B\left(\frac{Fea}{\sigma}\right)^2} - 1\right)\right]. \tag{9}$$

The dependence of μ on carrier concentration c is, for not too high c, only determined by the shape of the DOS [33], which is in all cases Gaussian. This dependence is very well described by Eqs. (6) and (7). We therefore concentrate on the T and F dependence at a low carrier concentration $c = 10^{-6}$. Figures 5–7 give for α-NPD, TCTA, and Spiro-DPVBi, respectively, and for various values of the dimensionless disorder strength $\hat{\sigma} \equiv \sigma/k_BT$ the dependence of μ on the dimensionless electric field Fea/σ, where $a = N_t^{-1/3}$ is the average center-to-center distance between the molecules and e the unit charge. The fits (curves) to the data (symbols) were obtained with a least-square procedure, taking into account only data for $Fea/\sigma \leqslant 1$, which is the typical electric field range relevant for device applications. We chose to fix the parameter A in Eq. (9) to $A = 0.30$ and optimize the parameters μ_0^* and C in Eq. (8), and the parameter B in Eq. (9). As can be observed, this provided in all cases good fits. The fitted parameters are given in Table II.

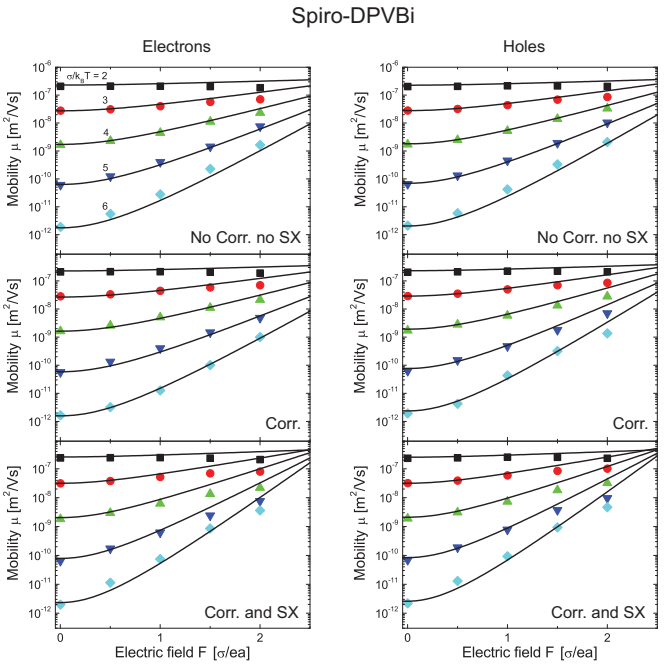

FIG. 7. Same as Fig. 5, but for Spiro-DPVBi.

TABLE II. The parameters in fits of the parametrization scheme, Eqs. (5)–(9), for the mobility function $\mu(T,c,F)$ of electrons and holes to the master-equation results in Figs. 5–7 for the three considered materials. The parameter A is 0.30 in all cases. The three considered cases are those where neither spatial energy correlations nor superexchange is included (no Corr. no SX), only correlations included (Corr.), and both correlations and superexchange included (Corr. and SX).

Material	Carrier	Case	μ_0^* [10^{-6} m^2/Vs]	C	B	AB
α-NPD	Electron	No Corr. no SX	12.1	0.41	1.0	0.30
α-NPD	Electron	Corr.	12.1	0.41	1.1	0.33
α-NPD	Electron	Corr. and SX	17.6	0.39	2.0	0.60
α-NPD	Hole	No Corr. no SX	2.5	0.42	1.3	0.39
α-NPD	Hole	Corr.	2.5	0.42	1.7	0.51
α-NPD	Hole	Corr. and SX	2.8	0.41	2.8	0.84
TCTA	Electron	No Corr. no SX	10.8	0.40	1.0	0.30
TCTA	Electron	Corr.	10.9	0.40	1.2	0.36
TCTA	Electron	Corr. and SX	18.3	0.39	2.1	0.63
TCTA	Hole	No Corr. no SX	6.1	0.41	1.9	0.57
TCTA	Hole	Corr.	6.2	0.40	2.0	0.60
TCTA	Hole	Corr. and SX	7.6	0.40	2.7	0.81
Spiro-DPVBi	Electron	No Corr. no SX	1.1	0.42	1.6	0.48
Spiro-DPVBi	Electron	Corr.	1.1	0.42	1.6	0.48
Spiro-DPVBi	Electron	Corr. and SX	1.2	0.41	2.4	0.63
Spiro-DPVBi	Hole	No Corr. no SX	1.1	0.41	1.7	0.52
Spiro-DPVBi	Hole	Corr.	1.1	0.41	1.9	0.57
Spiro-DPVBi	Hole	Corr. and SX	1.2	0.41	2.5	0.75

It follows from the results in Table II that including spatial energy correlations and superexchange leads to only a small decrease of the temperature dependence, but an appreciable increase of the field dependence of both the electron and hole mobilities in the three considered materials. In the last column of Table II, we report the product AB, which is a measure of the field sensitivity of the mobility at low field, where $\ln \mu$ is proportional to ABF^2. It appears that, in general, including superexchange has a stronger influence on the field dependence than including spatial energy correlations, since the enhancement in AB by adding superexchange is generally larger than that by adding correlations.

VI. HOMO–LUMO ENERGY CORRELATIONS

As mentioned in the introduction, the size and sign of the correlation between the on-site HOMO and LUMO energies have an important impact on the exciton formation rate [23]. Figure 8 shows in a scatter plot for all molecular sites in microscopic *ab initio* calculations for the three considered materials the values of $\Delta E_{\mathrm{LUMO}} \equiv E_{\mathrm{LUMO}} - \langle E_{\mathrm{LUMO}} \rangle$ versus $\Delta E_{\mathrm{HOMO}} \equiv E_{\mathrm{HOMO}} - \langle E_{\mathrm{HOMO}} \rangle$, where $\langle E_{\mathrm{LUMO}} \rangle$ and $\langle E_{\mathrm{HOMO}} \rangle$ are the average LUMO and HOMO energies. The *ab initio* calculations allow a separation of the LUMO and HOMO energies into a contribution due to the particular conformation of the considered molecule in the amorphous morphology and a contribution due to the Coulomb interaction of the electron or hole with the surrounding partial charges, which includes the change in these partial charges due to the presence of the electron or hole, i.e., polarization effects. The left and middle panels in Fig. 8 are scatter plots of the conformational and Coulombic contribution, respectively, and the right panels show the total results. We also provide the Pearson product-moment correlation coefficients for all cases (see the numbers in the panels). In Table III we report the standard deviations of the data shown in Fig. 8. We also report the square root of the quadratic sum of the standard deviations of the conformational and Coulombic contribution. In most cases, we note a slight discrepancy with the total standard deviation σ, which should be due to a small correlation between the conformational and Coulombic contribution to the energy.

It can be clearly observed that the HOMO and LUMO energies are positively correlated for α-NPD and TCTA, but negatively correlated for Spiro-DPVBi. The separation into the conformational and Coulombic contributions reveals the cause for this different behavior. The positive correlation in the cases of α-NPD and TCTA is governed by the positive correlation in the Coulombic contribution; see Figs. 8(b) and 8(e). We attribute this correlation to the electrostatic Coulomb interaction between an electron or a hole on a molecule and the static contribution to the partial charges in the environment, since a high electrostatic potential for an electron implies a low electrostatic potential energy for a hole and vice versa. Fluctuations in the polarizability of the environment due to the polarization contribution to the partial charges will have an opposite effect, with a high local polarizability decreasing both the potential energy of an electron and a hole, but this effect is not strong enough to counteract the electrostatic effect. The absence of a significant correlation in the conformational contribution in the cases of α-NPD and TCTA is mainly caused by the relative insensitivity of the LUMO energy to the molecular conformation as compared to the HOMO energy; see Figs. 8(a) and 8(d). The difference can be explained from an analysis of the spatial structures of the HOMO and LUMO, displayed in Figs. 1(a)–1(d) for the molecules in vacuum. It is observed that the HOMO is spread over the whole α-NPD or TCTA molecule, while

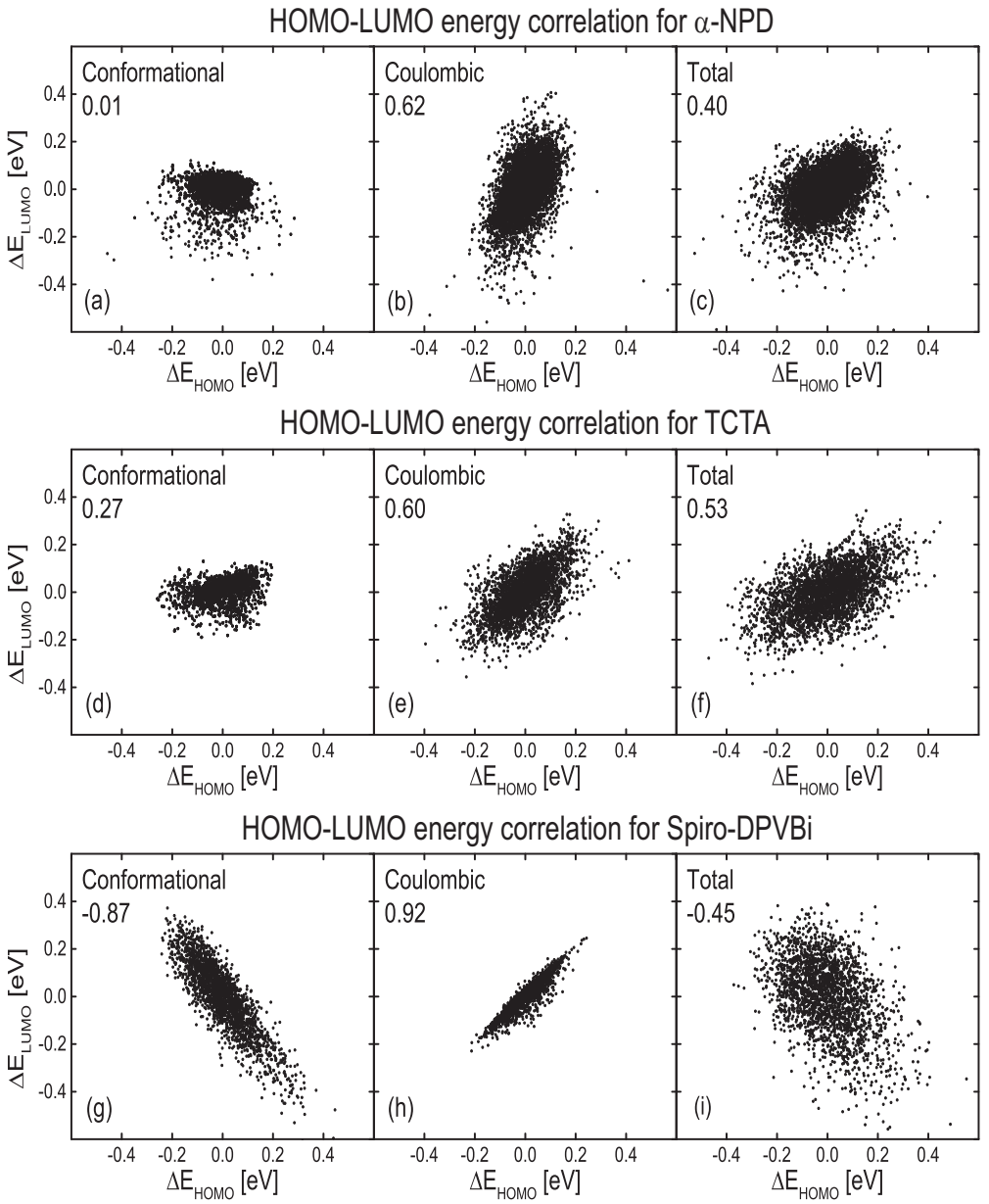

FIG. 8. Scatter plots of ΔE_{LUMO} vs ΔE_{HOMO} for α-NPD, TCTA, and Spiro-DPVBi, as following from microscopic *ab initio* calculations. The energies of 7225, 3196, and 2205 molecular sites were considered, respectively. In the left panels, only the conformational contribution to the HOMO and LUMO energies was included and in the middle panels only the Coulombic contribution. The right panels show the total results. The Pearson product-moment correlation coefficients are given in each panel.

the LUMO is more confined to parts of the molecule, an effect that is particularly pronounced in the case of α-NPD. As a consequence, the HOMO energy is more sensitive to changes in the conformation of the molecule than the LUMO energy.

The negative HOMO−LUMO energy correlation in the case of Spiro-DPVBi is dominated by a strongly negative correlation in the conformational contribution; see Fig. 8(g). The Coulombic contribution shows a strong positive correlation (of which the origin is likely the same as in the cases of α-NPD and TCTA), but due to its relatively small standard deviation (see Table III), this contribution is not sufficient to counteract the conformational contribution.

In order to determine the cause for the strongly negative conformational correlation between the HOMO and LUMO energies in Spiro-DPVBi, we analyzed the dependence of the energies and spatial structures of the HOMO and LUMO on the dihedral angle between the diphenylvinyl groups and the Spiro-bifluorene framework, related to rotations about the bonds indicated by the green spheres in Fig. 9(a). It was shown that for several molecular semiconductors there is a correlation between these dihedral rotations and energetic disorder [34]. These rotations are also the main cause for the conformational energy disorder in the amorphous structure of Spiro-DPVBi. Figure 9(b) shows the HOMO−1, HOMO, LUMO, and LUMO+1 energies of the Spiro-DPVBi molecule in vacuum as a function of one of the dihedral angles, while allowing

TABLE III. Standard deviations σ_{Conf} and σ_{Coul} of the conformational and Coulombic contributions to the LUMO and HOMO energies. The square root of the quadratic sum of the two contributions and the overall standard deviation σ are also given.

Material	Molecular orbital	σ_{Conf} [eV]	σ_{Coul} [eV]	$\sqrt{\sigma_{\text{Conf}}^2+\sigma_{\text{Coul}}^2}$ [eV]	σ [eV]
α-NPD	LUMO	0.048	0.075	0.089	0.087
α-NPD	HOMO	0.063	0.061	0.089	0.087
TCTA	LUMO	0.053	0.098	0.111	0.100
TCTA	HOMO	0.088	0.096	0.130	0.136
Spiro-DPVBi	LUMO	0.146	0.068	0.161	0.156
Spiro-DPVBi	HOMO	0.103	0.065	0.122	0.122

the other degrees of freedom of the molecule to relax to their equilibrium values. We observe from this figure a strong correlation between the HOMO and LUMO energies, where a high HOMO energy correlates with a low LUMO energy and vice versa. It is this negative correlation that leads to the strong conformational correlation between the HOMO and LUMO energies in the amorphous structure of Spiro-DPVBi, in which many different values of the dihedral angles occur. The dihedral angles in the microscopically calculated amorphous structure of Spiro-DPVBi are distributed as shown in Fig. 10, with a primary peak around 60° and a secondary peak around 120°.

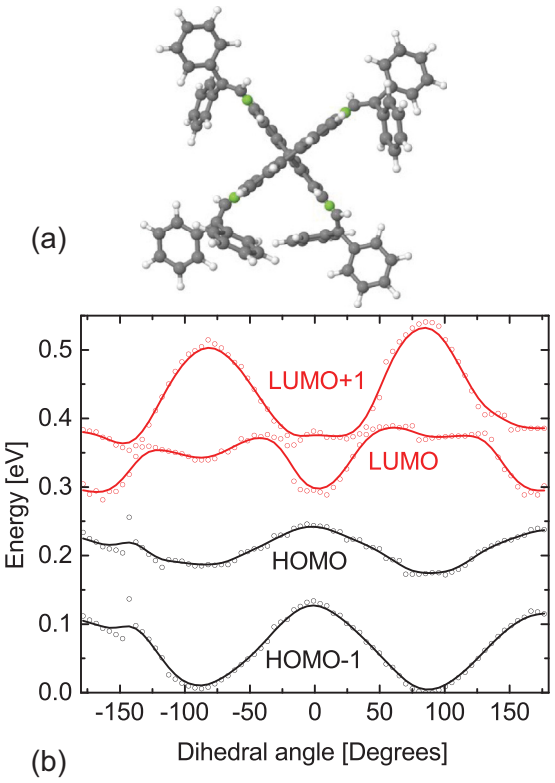

FIG. 9. (a) Structure of the Spiro-DPVBi molecule in vacuum. We study the changes in the energies and spatial structures of the HOMO and LUMO caused by a change of the dihedral angles related to rotations about the bonds indicated by the green spheres. (b) Dependence of the HOMO−1, HOMO, LUMO, and LUMO+1 energies of the Spiro-DPVBi molecule in vacuum on one of the dihedral angles indicated in (a), while allowing the other degrees of freedom of the molecule to relax. For visualization purposes, different offsets have been applied to the LUMO and LUMO+1 energies as compared to the HOMO and HOMO−1 energies. The lines are smooth fits to the calculated data (circles).

The behavior of the energies in Fig 9(b) can be understood as follows. For the case of the LUMO and LUMO+1, the coupling between the two equivalent parts of the Spiro-DPVBi molecule is very weak. As a consequence, the LUMO and LUMO+1 each localize on one part of the molecule; see Fig. 1(f) for the case of the LUMO. One of them reacts strongly to the dihedral angle that is changed, while the other does not. When this dihedral angle is 0°, the LUMO is maximally delocalized and its energy is lowest. Upon increase of the dihedral angle, the LUMO gets more localized and its energy increases until it reaches the energy of the LUMO+1 at about 40°. Beyond this angle, the roles of LUMO and LUMO+1 are reversed. The HOMO and HOMO−1 show a different behavior, because they are both delocalized over the whole molecule due to a strong coupling between the equivalent parts of the molecule; see Fig. 1(e) for the case of the HOMO. As a consequence, both HOMO and HOMO−1 react strongly to the dihedral angle that is changed. When this dihedral angle is 0°, they are both maximally delocalized and their energies are highest. Upon increase of the dihedral angle, both HOMO and HOMO+1 get more localized and their energies decrease. Because of the strong coupling between the equivalent parts of the molecule the HOMO and HOMO+1 do not cross each other.

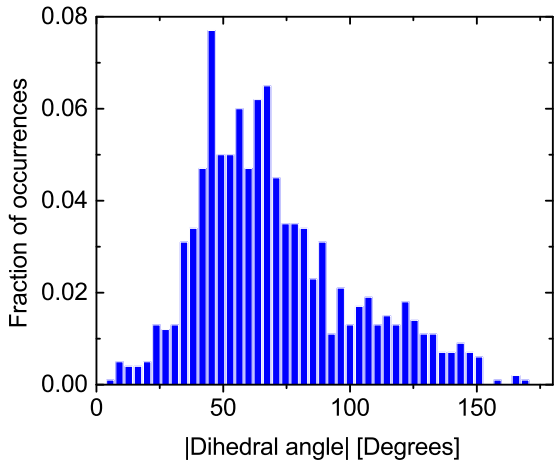

FIG. 10. Distribution of the absolute values of the dihedral angles of 1000 Spiro-DBVBi molecules in a microscopically calculated amorphous structure at 300 K.

VII. SUMMARY, CONCLUSIONS, AND DISCUSSION

In the first part of this paper, we have investigated the effects of spatial energy correlations and superexchange on the mobility functions of electrons and holes in three amorphous molecular semiconductors frequently applied in OLEDs: α-NPD, TCTA, and Spiro-DPVBi. The results were obtained from master-equation calculations based on a stochastic expansion of microscopic information obtained from *ab initio* morphology and electronic structure calculations. We concluded that the temperature dependence of the mobilities is slightly weakened and that the dependence on electric field is significantly enhanced, in particular when including superexchange.

We can now address the question whether the enhanced field dependence can explain the too weak voltage dependence found in the modeling of the temperature-dependent current density-voltage characteristics of hole-only α-NPD devices. As an example, we consider the injection-limited ITO|α-NPD|Pd devices studied in Ref. [7]. For the device with an α-NPD layer thickness of 100 nm, the largest difference occurred at the lowest temperature of 232 K and the highest voltage of 5 V, where the measured current density is larger than the modeled one by a factor of about 2.5 (see Fig. 8 in Ref. [7]). Since in injected-limited devices the electric field is approximately constant, we obtain the electric field by dividing the voltage by the layer thickness. Taking $\sigma = 0.1$ V, as in Ref. [7], and $a \approx 1$ nm, we find a dimensionless electric field Fea/σ of about 0.5. Using the parameters $A = 0.30$ and B from Table II, the field enhancement factor $f(T,F)$ in Eq. (9) is then about 2.4 when spatial energy correlations and superexchange are neglected, as in Ref. [7], and about 6.6 when they are taken into account. The extra enhancement by including spatial energy correlations and superexchange is thus a factor of about $6.6/2.4 \approx 2.8$, which is quite close to the required factor of 2.5. We can therefore conclude that the neglect of spatial energy correlations and especially superexchange could very well be responsible for the too weak voltage dependence in the modeling of the α-NPD devices in Refs. [7,10].

It also follows from the results in Table II that there are no qualitative differences between the mobility functions for electrons and holes in the three investigated materials. Remarkably, we conclude that the intrinsic electron mobilities in the "hole transporters" α-NPD and TCTA should be even larger than the hole mobilities. This means that if electron traps in these materials can be avoided and the problem of electron injection into these materials can be solved, they should also be able to serve as electron transporters. In Spiro-DPVBi, the intrinsic electron and hole mobilities are virtually the same. Hence, if electron trapping in this material can be avoided, it will be an interesting material for applications that require balanced electron and hole transport.

In the second part of this paper, we have investigated, using the results of the microscopic *ab initio* calculations, the on-site correlations between the molecular HOMO and LUMO energies in the three considered materials. We made a separation into a contribution due to the specific conformation of the molecule on which a charge resides and a contribution due to Coulomb interactions of the charge with the partial charges in its environment. We found that in α-NPD and TCTA the Coulombic contribution dominates, leading to a positive correlation between on-site HOMO and LUMO energies: an energetically favorable site for an electron is in general an energetically unfavorable site for a hole and vice versa. By contrast, we found that in Spiro-DPVBi the conformational contribution dominates, leading to a negative correlation between on-site HOMO and LUMO energies: an energetically favorable site for an electron is in general also an energetically favorable site for a hole and vice versa. The strong conformational contribution to the on-site HOMO−LUMO energy correlations in Spiro-DPVBi was explained by considering the effects of dihedral rotations in the Spiro-DPVBi molecule on the spatial structure and the energies of the frontier orbitals.

The size and sign of the on-site HOMO−LUMO energy correlation is of importance for the rate of exciton formation [23]. The positive correlation found in α-NPD and TCTA slows down exciton formation, because of an increased probability that electrons and holes get trapped at different sites. The negative correlation found in Spiro-DPVBi counteracts this effect, leading to an enhanced exciton formation rate. These results show the importance of molecular design in increasing exciton formation rates in molecular semiconductors.

ACKNOWLEDGMENTS

The research is part of the Dutch-German project "Modeling of Organic Light-Emitting Diodes: from Molecule to Device" (MODEOLED). On the Dutch side, it is supported by the Dutch Technology Foundation STW, the applied science division of NWO, and the Technology Program of the Dutch Ministry of Economic Affairs (project No. 12200). On the German side, it is supported by the "Deutsche Forschungsgemeinschaft" (DFG, Project No. WE1863/22-1). The research is also part of the Horizon 2020 EU projects EXTMOS (Contract No. 646176) and MOSTOPHOS (Contract No. 646259), and of the German project "Universelles Verständnis der Defekte in Materialien für die flexible Elektronik" (UNVEiL), funded by the German Federal Ministry of Education and Research (BMBF). The *ab initio* microscopic calculations were performed on the computational resource ForHLR Phase I, funded by the German Ministry of Science, Research and the Arts Baden-Württemberg, and the DFG. We thank René Janssen, Harm van Eersel, Siebe van Mensfoort, and Xander de Vries for many stimulating discussions.

[1] J. J. Kwiatkowski, J. Nelson, H. Li, J. L. Bredas, W. Wenzel, and C. Lennartz, Phys. Chem. Chem. Phys. **10**, 1852 (2008).

[2] V. Rühle, A. Lukyanov, F. May, M. Schrader, T. Vehoff, J. Kirkpatrick, B. Baumeier, and D. Andrienko, J. Chem. Theory Comput. **7**, 3335 (2011).

[3] A. Fuchs, T. Steinbrecher, M. S. Mommer, Y. Nagata, M. Elstner, and C. Lennartz, Phys. Chem. Chem. Phys. **14**, 4259 (2012).
[4] T. Neumann, D. Danilov, C. Lennartz, and W. Wenzel, J. Comput. Chem. **34**, 2716 (2013).
[5] P. Friederich, F. Symalla, V. Meded, T. Neumann, and W. Wenzel, J. Chem. Theory Comput. **10**, 3720 (2014).
[6] P. Kordt, J. J. M. van der Holst, M. Al Helwi, W. Kowalsky, F. May, A. Badinski, C. Lennartz, and D. Andrienko, Adv. Funct. Mater. **25**, 1955 (2015).
[7] A. Massé, P. Friederich, F. Symalla, F. Liu, R. Nitsche, R. Coehoorn, W. Wenzel, and P. A. Bobbert, Phys. Rev. B **93**, 195209 (2016).
[8] W. F. Pasveer, J. Cottaar, C. Tanase, R. Coehoorn, P. A. Bobbert, P. W. M. Blom, D. M. de Leeuw, and M. A. J. Michels, Phys. Rev. Lett. **94**, 206601 (2005).
[9] H. Bässler, Phys. Status Solidi B **175**, 15 (1993).
[10] F. Liu, A. Massé, P. Friederich, F. Symalla, R. Nitsche, W. Wenzel, R. Coehoorn, and P. A. Bobbert, Appl. Phys. Lett. **109**, 243301 (2016).
[11] G. Schwartz, T.-H. Ke, C.-C. Wu, K. Walzer, and K. Leo, Appl. Phys. Lett. **93**, 073304 (2008).
[12] S. W. Tsang, M. W. Denhoff, Y. Tao, and Z. H. Lu, Phys. Rev. B **78**, 081301 (2008).
[13] Y. Gartstein and E. Conwell, Chem. Phys. Lett. **245**, 351 (1995).
[14] S. V. Novikov, D. H. Dunlap, V. M. Kenkre, P. E. Parris, and A. V. Vannikov, Phys. Rev. Lett. **81**, 4472 (1998).
[15] M. Bouhassoune, S. L. M. van Mensfoort, P. A. Bobbert, and R. Coehoorn, Org. Elec. **10**, 437 (2009).
[16] B. Baumeier, O. Stenzel, C. Poelking, D. Andrienko, and V. Schmidt, Phys. Rev. B **86**, 184202 (2012).
[17] G. Schwartz, K. Fehse, M. Pfeiffer, K. Walzer, and K. Leo, Appl. Phys. Lett. **89**, 083509 (2006).
[18] M. Mesta, M. Carvelli, R. J. de Vries, H. van Eersel, J. J. M. van der Holst, M. Schober, M. Furno, B. Lüssem, K. Leo, P. Loebl, R. Coehoorn, and P. A. Bobbert, Nat. Mater. **12**, 652 (2013).
[19] N. Hush, Coord. Chem. Rev. **64**, 135 (1985).
[20] D. Segal, A. Nitzan, W. B. Davis, M. R. Wasielewski, and M. A. Ratner, J. Phys. Chem. B **104**, 3817 (2000).
[21] C. Lambert, G. Noll, and J. Schelter, Nat. Mater. **1**, 69 (2002).
[22] F. Symalla, P. Friederich, A. Massé, V. Meded, R. Coehoorn, P. Bobbert, and W. Wenzel, Phys. Rev. Lett. **117**, 276803 (2016).
[23] J. J. M. van der Holst, F. W. A. van Oost, R. Coehoorn, and P. A. Bobbert, Phys. Rev. B **80**, 235202 (2009).
[24] P.-O. Löwdin, J. Chem. Phys. **18**, 365 (1950).
[25] V. Stehr, J. Pfister, R. F. Fink, B. Engels, and C. Deibel, Phys. Rev. B **83**, 155208 (2011).
[26] R. Ahlrichs, M. Bär, M. Häser, H. Horn, and C. Kölmel, Chem. Phys. Lett. **162**, 165 (1989).
[27] A. D. Becke, J. Chem. Phys. **98**, 1372 (1993).
[28] A. Schäfer, H. Horn, and R. Ahlrichs, J. Chem. Phys. **97**, 2571 (1992).
[29] S. F. Nelsen, S. C. Blackstock, and Y. Kim, J. Am. Chem. Soc. **109**, 677 (1987).
[30] A. Schäfer, C. Huber, and R. Ahlrichs, J. Chem. Phys. **100**, 5829 (1994).
[31] R. Thiedmann, I. Manke, W. Lehnert, and V. Schmidt, J. Mater. Sci. **46**, 7745 (2011).
[32] R. A. Marcus, Rev. Mod. Phys. **65**, 599 (1993).
[33] J. Cottaar, L. J. A. Koster, R. Coehoorn, and P. A. Bobbert, Phys. Rev. Lett. **107**, 136601 (2011).
[34] P. Friederich, V. Meded, A. Poschlad, T. Neumann, V. Rodin, V. Stehr, F. Symalla, D. Danilov, G. Lüdemann, R. F. Fink, I. Kondov, F. von Wrochem, and W. Wenzel, Adv. Funct. Mater. **26**, 5757 (2016).